J. Fluid Mech. (1997), *vol.* 348, *pp.* 1–28. Printed in the United Kingdom

Instabilities and bifurcation of non-equilibrium two-phase flows

By STEPHAN ADAM AND GÜNTER H. SCHNERR

Institut für Strömungslehre und Strömungsmaschinen, Universität Karlsruhe (TH), Kaiserstraße 12, D-76128 Karlsruhe, Germany

(Received 4 June 1996 and in revised form 11 December 1996)

New instabilites of unsteady transonic flows with non-equilibrium phase transition are presented including unsymmetric flow patterns with moving oblique shock systems in supersonic nozzles with perfectly symmetric shapes. The phenomena were first detected when performing experiments in our supersonic wind tunnel with atmospheric supply and could be perfectly reproduced by numerical simulations based on the Euler equations, i.e. neglecting the viscosity of the fluid. The formation of the liquid phase is modelled using the classical nucleation theory for the steady state together with the Hertz–Knudsen droplet growth law and yields qualitatively and quantitatively excellent agreement with experiments in the unsteady flow regime with high-frequency oscillations including the unstable transient change of the structure from symmetric to unsymmetric flow.

For engineering applications the sudden increase or decrease of the frequency by a factor 2 or more and of the pressure amplitude at the bifurcation limits is of immediate practical interest, e.g. for flutter excitation of turbomachinery blading.

1. Introduction

Phase transition of vapour or vapour/carrier gas mixtures from the gaseous to the liquid phase by condensation occurs in equilibrium only if the cooling process is very slow. In this case the metastable supersaturated state is prevented by the presence of a significant number of foreign condensation nuclei (e.g. ions, aerosols, particles) or surfaces. Homogeneous nucleation, where the condensation nuclei form in the vapour phase itself, prevails if the characteristic timescale of the cooling is small compared to the timescale of the agglomeration of vapour molecules at pre-existing nuclei. Therefore, in flows with fast expansions the development of the liquid phase is dominated by homogeneous condensation. If, as in many internal flows of water vapour, the cooling rate of the expansion $-\mathrm{d}T/\mathrm{d}t$ is of the order $1\,^{\circ}\mathrm{C}\ \mu\mathrm{s}^{-1}$, heterogeneous condensation effects can be neglected. Typical water-vapour concentrations in the supply lead to transonic condensation onset Mach numbers, where the flow is near the maximum mass flux density and very sensitive to small changes, e.g. the release of latent heat from condensation. For excessive heat release the flow immediately becomes thermally choked (Delale, Schnerr & Zierep 1993*a*), and phenomena like supercritical heat addition with steady shocks and different modes of self-excited periodic oscillations

at frequencies typically in the range of about 1 kHz alter the flow pattern completely.

The phenomenon of self-excited oscillations in slender nozzle flows of moist air was discovered by Schmidt (1962). Barschdorff (1967, 1971) continued this research and obtained experimentally quantitative results for the frequency of homogeneously condensing flows of moist air and pure steam. He found a monotonically increasing frequency dependence on the water-vapour content in the supply. The first similarity law for the dimensionless frequency of self-excited oscillations was derived by Zierep & Lin (1968) for a constant nozzle throat height, different expansion rates and varying supply conditions. Subsequently, experimental results for unsteady pure steam flows were presented by Barschdorff & Filippov (1970), Deych *et al.* (1974), Wegener & Cagliostro (1973), and Matsuo *et al.* (1983, 1985) using either supersonic wind tunnels or Ludwieg tubes.

The first numerical results for unsteady two-phase nozzle flows with non-equilibrium condensation of water vapour obtained with a one-dimensional code were presented by Saltanov & Tkalenko (1975) and compared with experiments. Here two oscillation modes (which we will denote by 1 and 2) were presented. In the first mode a shock caused by condensation moves upstream and disappears in the oncoming subsonic flow, whereas the oscillation is restricted to the divergent nozzle section in the second mode. Skillings & Jackson (1987) applied Lagrangian integration of the one-dimensional equations of pure steam flow in order to track the development of up to 25 droplet groups and determined the unsteady droplet spectrum. Numerical simulations of the two different oscillation modes were also presented by Guha & Young (1991). Recently Collignan (1994) obtained a frequency minimum in wet-steam nozzle flow with a one-dimensional Euler code, even though the calculated frequencies were higher than from experiments.

An important step forward was the first two-dimensional calculation of unsteady wet-steam flow by White & Young (1993). In a slender Laval nozzle with nearly normal shocks a bimodal droplet distribution forms instantaneously within the oscillation period. The frequency difference between experiment and numerical simulation in the presented case is about 10%. Šejna (1993) investigated the same slender nozzle to compare one-dimensional and two-dimensional calculations, which demonstrated the known effect of frequency decrease by two-dimensional wave phenomena, here of about 15%.

Mundinger (1994) recently developed a numerical scheme of high accuracy for the calculation of two-dimensional unsteady flow of water vapour/carrier gas mixtures in strongly curved nozzles with the highest accuracy, having typical errors of 5% for the frequency. This method has been applied to a systematic investigation of the frequency dependence on all relevant parameters in circular arc nozzle flows, i.e. the nozzle geometry, the time-scale of the expansion and the reservoir conditions (Schnerr, Adam & Mundinger 1994*a*, *b*; Schnerr *et al.* 1995).

2. Dynamics of self-excited flow oscillations

Depending on the nozzle geometry there exist different types of self-excited flow oscillations caused by homogeneous condensation. Before the detailed investigation of the different flow oscillations is discussed below, a comparison of the different dynamics observed is depicted. Figure 1 shows the structure of the frequency dependence for three different nozzle geometries depending on the relative hu-

midity in the supply, i.e. $\Phi_0 = p_{v,0}/p_{s,\infty}(T_{01})$. Here $p_{v,0}$ is the water-vapour partial pressure in the supply and $p_{s,\infty}$ is the saturation pressure for a plane boundary at the reservoir temperature T_{01}, which is kept constant (295 K). In the diagrams numerical results are shown which are in good agreement with our experiments.

In a slender circular arc nozzle (S2) with a nearly constant temperature gradient $-\mathrm{d}T/\mathrm{d}x$ we obtain a sharp frequency minimum (figure 1*a*). Near the stability limit between steady-state and unsteady flow ($\Phi_0 = 68\%$) the frequency increases with decreasing Φ_0. In this regime the flow oscillation is restricted to an oscillation of a normal shock with very low amplitude. Thus the transition to steady-state flow occurs with vanishing amplitude of the shock motion and finite frequency. Before, it was assumed that the frequency decreases monotonically toward the stability limit to steady-state flow (Barschdorff 1967). Between the stability limit and the frequency minimum the flow is highly sensitive to small changes in Φ_0. An increase in Φ_0 of less than 5% results in a decrease of the frequency from 1030 Hz to values below 600 Hz.

The effects of higher curvature of the nozzle walls and therefore of the streamlines are demonstrated in figure 1(*b*). In a nozzle with high wall curvature S1, which has the same temperature gradient $-(\mathrm{d}T/\mathrm{d}x)^*_{1-D} = 8.14$ K cm^{-1} according to one-dimensional theory as nozzle S2, strong two-dimensional effects become apparent. For low values of Φ_0 the flow tends to be stabilized. Thus the stability limit is shifted to higher values ($\Phi_0 = 74\%$). Above the stability limit the frequency decreases compared to nozzle S2 for low Φ_0. The strong minimum disappears and depending on the reservoir temperature T_{01} we observe one or two frequency minima. The two-dimensional effects on the frequency become less important for high values of Φ_0 where the curve approaches that of nozzle S2.

The last example shows a nozzle with a very low geometrical divergence which leads to a constant outflow Mach number of 1.2 in isentropic flow (figure 1*c*). The temperature gradient at the throat of the nozzle is $-(\mathrm{d}T/\mathrm{d}x)^*_{1-D} = 5.43$ K cm^{-1}, but here it decreases with a strong nonlinearity toward the exit of the nozzle, whereas it is nearly constant in the circular arc nozzles. The frequency diagram shows a completely different, yet unresolved structure. A bifurcation of the frequency curve with a regime of hysteresis is observed. For $\Phi_0 > 68.0\%$, we suddenly obtain two branches of the frequency curve in completely different frequency regimes. The frequency suddenly jumps by a factor two or more from values between 200 and 450 Hz on the lower branch to values above 750 Hz. Increasing Φ_0 along the lower branch is only possible for values below 95%. Then the flow suddenly gets into another, yet unresolved, oscillation mode which will be discussed below. The frequency increases from 447 Hz ($\Phi_0 = 90\%$) to 1118 Hz ($\Phi_0 = 95\%$). Decreasing Φ_0 again along this branch yields high frequencies until a value of 68.5% is reached. Below this limit the flow again changes completely, returns to the original oscillation mode and the frequency jumps from 758 Hz ($\Phi_0 = 68.5\%$) down to 387 Hz ($\Phi_0 = 68.4\%$).

In this nozzle the stability limit for steady-state flow is shifted to much lower values of Φ_0. This is caused by the lower temperature gradient and the geometry, which allows only a very low amount of heat to be released to the flow in steady state.

After this discussion of the dynamics of self-excited flow oscillations in different geometries, we present detailed investigations of the corresponding flow fields.

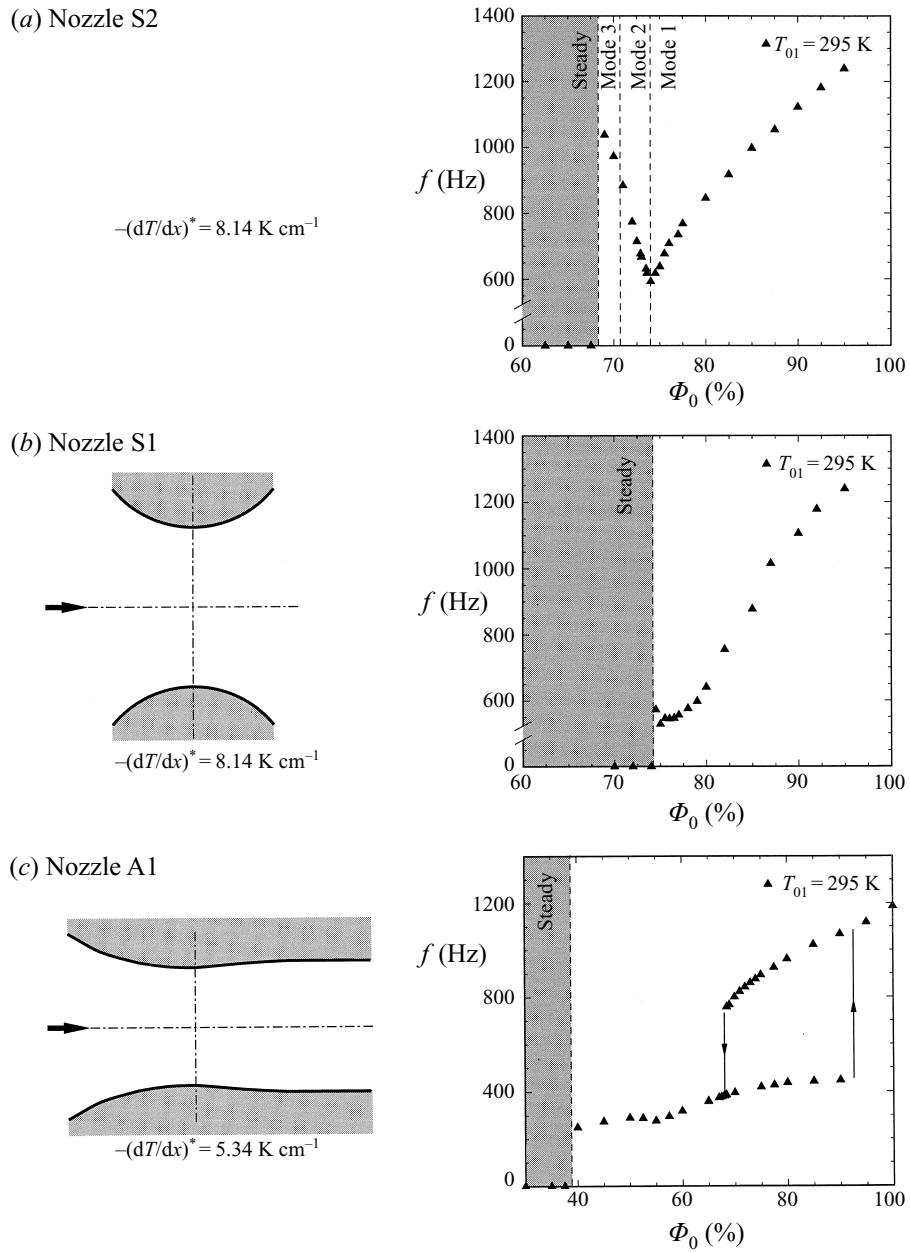

FIGURE 1. Dynamics of self-excited flow oscillations. Frequency dependence for (*a*) slender circular arc nozzle S2 (throat height $2y^* = 30$ mm, radius of wall curvature $R^* = 400$ mm), (*b*) strongly curved circular arc nozzle S1 ($2y^* = 120$ mm, $R^* = 100$ mm), and (*c*) nozzle with parallel outflow A1 ($2y^* = 90$ mm, radius of wall curvature at the throat $R^* = 300$ mm, constant exit Mach number $M_{e,is.} = 1.2$ in isentropic flow).

3. Physical modelling and numerical scheme

3.1. *Physical modelling*

The two-phase flow is assumed to be inviscid, rotational, and two-dimensional. The assumption of inviscid flow holds for accelerated flows with weak shocks where the viscous effect reduces to the displacement effect of the boundary layer. As heat addition can be regarded as a displacement effect the boundary layers of the nozzle flows considered typically are not likely to separate. Even adiabatic experiments confirm that the shocks at Mach numbers between 1 and 1.25 do not induce separation.

The investigated vapour/carrier gas mixture consists of a large amount of dry air and a small amount of condensable water vapour. Typical mixing ratios are about 1%. Nevertheless, owing to the high latent heat of water, the increase in the stagnation enthalpy of the gaseous phase by homogeneous condensation is 10 times higher, about 10% of the reservoir value. Compared to this, heat transfer through thermal boundary layers can be neglected. Air and water vapour are treated as perfect gases. The small vapour mass and high cooling rates in the flow result in maximum droplet radii of about 5×10^{-8} m. Thus the governing equations can be simplified, i.e. the droplet volume and the slip between the gaseous phase and the droplets are negligible.

A rough estimation yields approximately 10^{-6} s for the timescale of the formation of a critical droplet. On the other hand, owing to the expansion, the temperature change of a fluid particle during this time is typically less than 1 K and the frequency of the flow oscillation is of the order 1 kHz, which gives a characteristic timescale of 10^{-3} s. As this flow timescale is large compared to the timescale of nucleation and the relative temperature change during the droplet formation is of the order 0.1 % the classical steady nucleation theory of Volmer, Frenkel and Zel'dovich is still appropriate (Delale & Schnerr 1996). Accordingly, calculation of the nucleation rate J, the rate of nuclei formation per unit volume per unit time, in the unsteady condensing flow field with

$$J = \left(\frac{2}{\pi}\frac{\sigma}{m^3}\right)^{1/2} \frac{\rho_v^2}{\rho_c} \exp\left[\frac{-16\pi\sigma^3}{3m\rho_c^2 R_v^3 T^3 \ln^2(\mathcal{S})}\right] \tag{3.1}$$

leads to good agreement with macroscopic experimental results. Here $\sigma, m, \rho_v, \rho_c, R_v, T$, and $\mathcal{S}$ are, respectively, the surface tension, the mass per molecule of the vapour, the densities of the vapour and the condensate, the specific gas constant of the vapour, the temperature, and the supersaturation $\mathcal{S} = p_v(T)/p_{s,\infty}(T)$. Besides the supersaturation $\mathcal{S}$, the most important quantity in (3.1) is the surface tension σ in the exponent to the third power. No definite statements can be made on the nature of the condensate (liquid or solid) at condensation onset temperatures far below the triple point, typically at $-50\,^{\circ}\mathrm{C}$ to $-60\,^{\circ}\mathrm{C}$. Therefore, the surface tension is handled as free parameter.

The critical droplet radius is defined by

$$r^* = \frac{2\sigma}{\rho_c R_v T \ln(\mathcal{S})}. \tag{3.2}$$

At condensation onset with maximum supersaturation (Wilson point) the smallest nuclei consist only of a few molecules, 10–20, and are less than one order larger than the molecule size. Numerical results compared to experiments show that the droplet radii remain smaller than the mean free path of the vapour/carrier gas mixture. Furthermore, for high mass fractions of the inert carrier gas of about 99% the heat conduction in the gaseous phase is strong enough to keep the temperature of the droplet and its environment in good approximation the same. Therefore, the energy

equation is redundant, i.e. the diffusion of the vapour molecules to the droplet surface controls the droplet growth, and the microscopic Hertz–Knudsen law

$$\frac{\mathrm{d}r}{\mathrm{d}t} = \frac{\alpha}{\rho_c}\frac{p_v - p_{s,r}}{(2\pi R_v T)^{1/2}} \tag{3.3}$$

is used to calculate the droplet growth. Here α, p_v, and $p_{s,r}$ represent the mass accommodation coefficient, the vapour pressure and the saturation pressure of a droplet of radius r. Detailed comparisons of steady nozzle flow experiments and numerical calculations have yielded empirical relationships for the surface tension σ and the mass accommodation coefficient α (Schnerr & Dohrmann 1990; Schnerr 1993), which are in agreement with the experiments of Peters & Paikert (1989).

With (3.1)–(3.3), the condensate formation is determined according to the formulation of Hill (1966) which leads to four conservation equations for the properties of the condensate using a surface-averaged droplet radius $\bar{r}$.

3.2. *Numerical scheme*

The two-phase flow of the water vapour/carrier gas mixture is calculated using the Euler equations and the four additional partial differential equations describing the condensate formation (Mundinger 1994; Schnerr *et al.* 1994*a*, *b*):

$$\frac{\partial \boldsymbol{U}}{\partial t} + \frac{\partial \boldsymbol{F}}{\partial x} + \frac{\partial \boldsymbol{G}}{\partial y} = \boldsymbol{S} \tag{3.4}$$

where

$$\boldsymbol{U} = \begin{pmatrix} \rho \\ \rho u \\ \rho v \\ \rho E \\ \rho g \\ \rho Q_2 \\ \rho Q_1 \\ \rho Q_0 \end{pmatrix}, \quad \boldsymbol{F} = \begin{pmatrix} \rho u \\ \rho u^2 + p \\ \rho uv \\ (\rho E + p)u \\ \rho g u \\ \rho Q_2 u \\ \rho Q_1 u \\ \rho Q_0 u \end{pmatrix}, \quad \boldsymbol{G} = \begin{pmatrix} \rho v \\ \rho uv \\ \rho v^2 + p \\ (\rho E + p)v \\ \rho g v \\ \rho Q_2 v \\ \rho Q_1 v \\ \rho Q_0 v \end{pmatrix},$$

$$\boldsymbol{S} = \begin{pmatrix} 0 \\ 0 \\ 0 \\ 0 \\ \frac{4}{3}\pi\rho_c \left(Jr^{*3} + 3\rho Q_2 \,\mathrm{d}\bar{r}/\mathrm{d}t\right) \\ Jr^{*2} + 2\rho Q_1 \,\mathrm{d}\bar{r}/\mathrm{d}t \\ Jr^{*} + \rho Q_0 \,\mathrm{d}\bar{r}/\mathrm{d}t \\ J \end{pmatrix}, \quad E = e + \frac{u^2 + v^2}{2}.$$

Here p, ρ, e, and E are, respectively, the static pressure, the density, the specific internal energy and the specific total internal energy of the mixture, u and v are the Cartesian components of the velocity vector. The condensate is represented by the condensate mass fraction g, i.e. the ratio of the mass of condensed water per unit mass of the mixture and the properties Q_0, Q_1, and Q_2 with

$$Q_0 = \int_{-\infty}^{t} \frac{J(\tau)}{\rho(\tau)}\mathrm{d}\tau, \quad Q_1 = \int_{-\infty}^{t} r(\tau)\frac{J(\tau)}{\rho(\tau)}\mathrm{d}\tau, \quad Q_2 = \int_{-\infty}^{t} r^2(\tau)\frac{J(\tau)}{\rho(\tau)}\mathrm{d}\tau. \tag{3.5}$$

The surface-averaged droplet radius is defined by $\bar{r} = (Q_2/Q_0)^{1/2}$ according to Hill (1966).

The release of latent heat is included in the internal energy e, which couples the phase transition process to the first four equations of the system (3.4). The non-equilibrium phase transition, nucleation, and condensate formation, are represented by the source term vector on the right-hand side of (3.4). In contrast to flows without condensation ($g = 0$), the speed of sound a in the mixture additionally depends on the condensate mass fraction g. The eigenvalues of the hyperbolic system of equations (3.4) give for the speed of sound the expression

$$a^2 = \left(\frac{\partial p}{\partial \rho}\right)_{e,g} + \frac{p}{\rho^2}\left(\frac{\partial p}{\partial e}\right)_{\rho,g}, \tag{3.6}$$

which is equal to the frozen speed of sound $a_f^2 = (\partial p/\partial \rho)_{s,g}$ with the specific entropy s. Assuming a linear approximation for the latent heat and appropriate values of the constants L_0 and L_1 within the temperature range $200 \leqslant T \leqslant 300$ K, namely $L(T) = L_0 + L_1 T$, it follows that

$$a^2 = a_f^2 = \Gamma \frac{p}{\rho} \qquad \text{with} \qquad \Gamma = \frac{c_{p0} - gL_1}{c_{v0} + g(R_v - L_1)} \tag{3.7}$$

where c_{p0} and c_{v0} are the specific heat at constant pressure and constant volume at $g = 0$, respectively.

On curvilinear body-fitted coordinates ξ and η the conservation equations (3.4) can be written as

$$\frac{1}{J}\frac{\partial \boldsymbol{U}}{\partial t} + \frac{\partial \hat{\boldsymbol{F}}}{\partial \xi} + \frac{\partial \hat{\boldsymbol{G}}}{\partial \eta} = \frac{1}{J}\boldsymbol{S}(\boldsymbol{U}). \tag{3.8}$$

Here $\hat{\boldsymbol{F}}$ and $\hat{\boldsymbol{G}}$ are the vectors of fluxes in the ξ- and η-directions and J is the determinant of the Jacobian matrix.

The system (3.8) is solved using a MUSCL-type finite volume method. A fractional step method is used to split the equations into an homogeneous and an inhomogeneous equation to account for different timescales of the flow and condensation process, respectively (Oran & Boris 1987):

$$\frac{1}{J}\frac{\partial \boldsymbol{U}^{(hom)}}{\partial t} + \frac{\partial \hat{\boldsymbol{F}}}{\partial \xi} + \frac{\partial \hat{\boldsymbol{G}}}{\partial \eta} = 0, \tag{3.9}$$

$$\frac{\partial \boldsymbol{U}}{\partial t} = \boldsymbol{S}(\boldsymbol{U}^{(hom)}). \tag{3.10}$$

Both equations are solved by explicit, second-order-accurate time integration. The time step Δt in the calculation of the homogeneous equation (3.9) follows from a CFL-criterion, whereas the inhomogeneous equation (3.10) is integrated by calculating the source terms in k time steps $\Delta t^{(\nu)}$ with $\Delta t = \sum_{\nu=1}^{k} \Delta t^{(\nu)}$. Here the time step $\Delta t^{(\nu)}$ is limited by a maximum value of the condensate mass $m_{c,max}$ formed in each cell, i.e.

$$\Delta t^{(\nu)} \frac{\mathrm{d}(\rho g)}{\mathrm{d}t} < m_{c,max} = \text{const.} \tag{3.11}$$

The fluxes at the cell interfaces $\hat{\boldsymbol{F}}(\boldsymbol{U})$ and $\hat{\boldsymbol{G}}(\boldsymbol{U})$ are determined by van Leer flux vector splitting for real gases using the frozen speed of sound (Shuen, Liou & van Leer 1990). The vector $\boldsymbol{U}$ at the cell interfaces is calculated via the κ-scheme by

van Leer using the van Albada limiter (Anderson, Thomas & van Leer 1986), which reduces the accuracy from third order in smooth regions to first order near shocks.

At the nozzle wall the boundary condition of Deconinck & Struys (1988) is applied. At the subsonic inflow boundary we prescribe the flow angle, total enthalpy, and entropy. In the case of supersonic outflow all variables are extrapolated from the interior at the outflow boundary, whereas the static pressure is prescribed for subsonic outflow.

Alternatively the steady adiabatic flow solution for dry air or the solution of a diabatic flow field with different reservoir conditions can be used as initial condition. At $t = 0$ the reservoir conditions are instantaneously replaced by the new values. In both cases a periodic solution of the flow is obtained after 5–6 transient oscillations.

The CPU time of the vectorized code to get periodic solutions is 5–10 min on our SNI S600/20 vector computer (measured performance of 1.8 GFLOPS). Typically the frequency difference of the solution in comparison with experimental values is 5%.

4. Experimental set-up

The experiments were carried out in our intermittent supersonic wind tunnel. Atmospheric moist air is sucked through the tunnel into a vacuum tank. The test section has a maximum cross-sectional area of 50×230 mm^2. Depending on the nozzle throat height the blowing time of the wind tunnel is 10–30 s.

Visualization of the two-dimensional flow field is performed with the schlieren technique using a sparc light source (Strobokin) with an exposure time of approximately 1 μs. The schlieren streak method is applied to register the dynamics of the shock motion along the nozzle axis. Here a narrow slit is projected onto a film rotating in a Strobodrum camera. The superposition of the shock and the film movements yields the time-dependent shock position, which can be analysed quantitatively by timing marks on the film.

The shape of the divergent part (length 88.7 mm) of nozzle A1 was determined with the method of characteristics leading to a constant outflow Mach number 1.2 in inviscid flow. Downstream the nozzle is prolongated with constant cross-sectional area (length 105.3 mm). For the Euler simulation this configuration was used. However, to obtain the constant outflow Mach number 1.2 in the experiment, it was neccessary to compensate the effect of the boundary layers at the nozzle and the wind tunnel walls. Therefore, the geometry used for the experiments was designed slightly divergent in such a manner that the displacement effect of the boundary layers and the divergence of the geometry cancel out in adiabatic flow. Behind the parallel part the cross-sectional area is discontinuously enlarged to the whole wind tunnel section.

The circular arc nozzles are the same in the experiment and in the numerical simulation because here the boundary layer displacement effect is less significant due to the stronger divergence of the geometry.

5. Quasi-one-dimensional flow oscillations

The frequency distribution for the slender, quasi-one-dimensional nozzle S2 in figure 1(*a*) shows a strong dependence on Φ_0 near the limit of stability, where the flow becomes steady. In this regime three different modes of oscillation can be distinguished as shown by schlieren streak photographs in figure 2. The flow comes from the left, time increases from the top. The white line indicates the shock position along the nozzle axis, the black line shows the throat of the nozzle. At the left (mode 1)

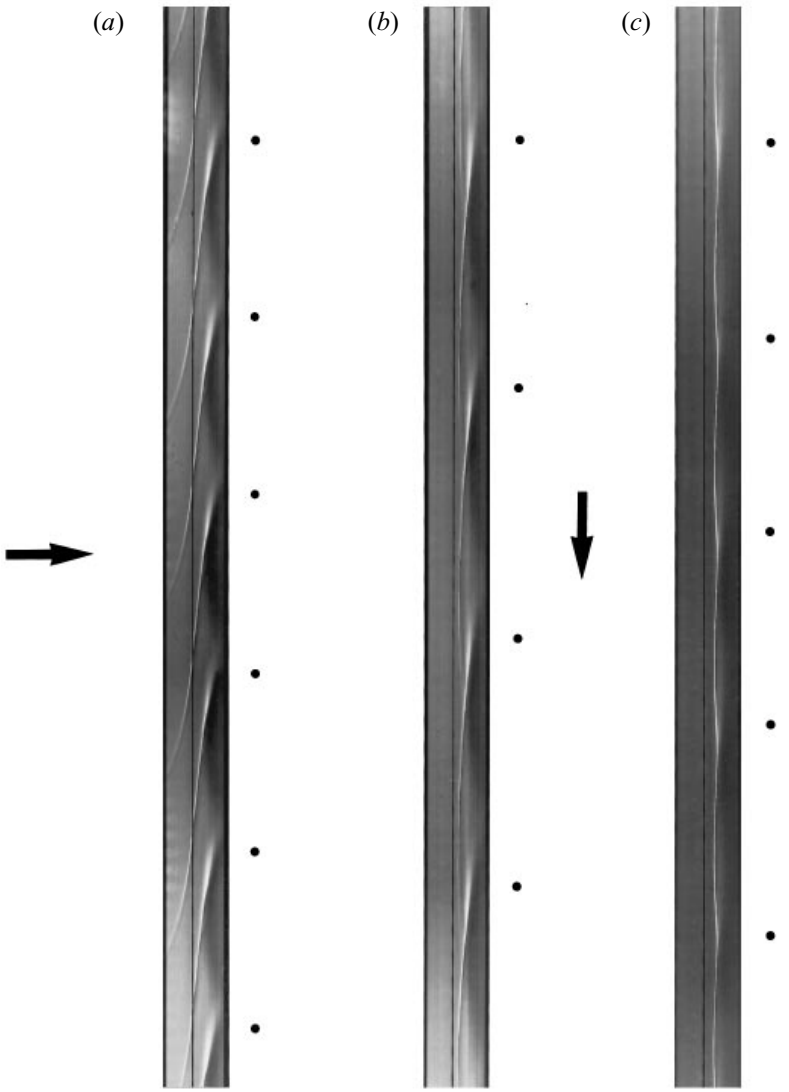

FIGURE 2. Schlieren streak photographs of mode 1, 2, and 3 in slender circular arc nozzle S2.

	$T_{01}\,(K)$	p_{01} (bar)	$\Phi_0\,(\%)$	$x\,(g_{H_2O}/kg_{dry\ air})$	f (Hz)
(*a*) mode 1	293.2	1.007	85.3	12.6	1013
(*b*) mode 2	292.8	1.007	78.5	11.3	742
(*c*) mode 3	297.5	1.005	75.6	14.6	956

a shock builds up periodically in the divergent nozzle section, it moves upstream, accelerates through the throat and weakens in the convergent nozzle section. Finally it disappears at the left end of the photograph in the oncoming flow and a new shock builds up downstream. In this mode the whole flow field is affected by the oscillation.

The streak photograph in the middle for a lower value of Φ_0 (mode 2) shows a similar situation, but here the shock stops before it reaches the nozzle throat,

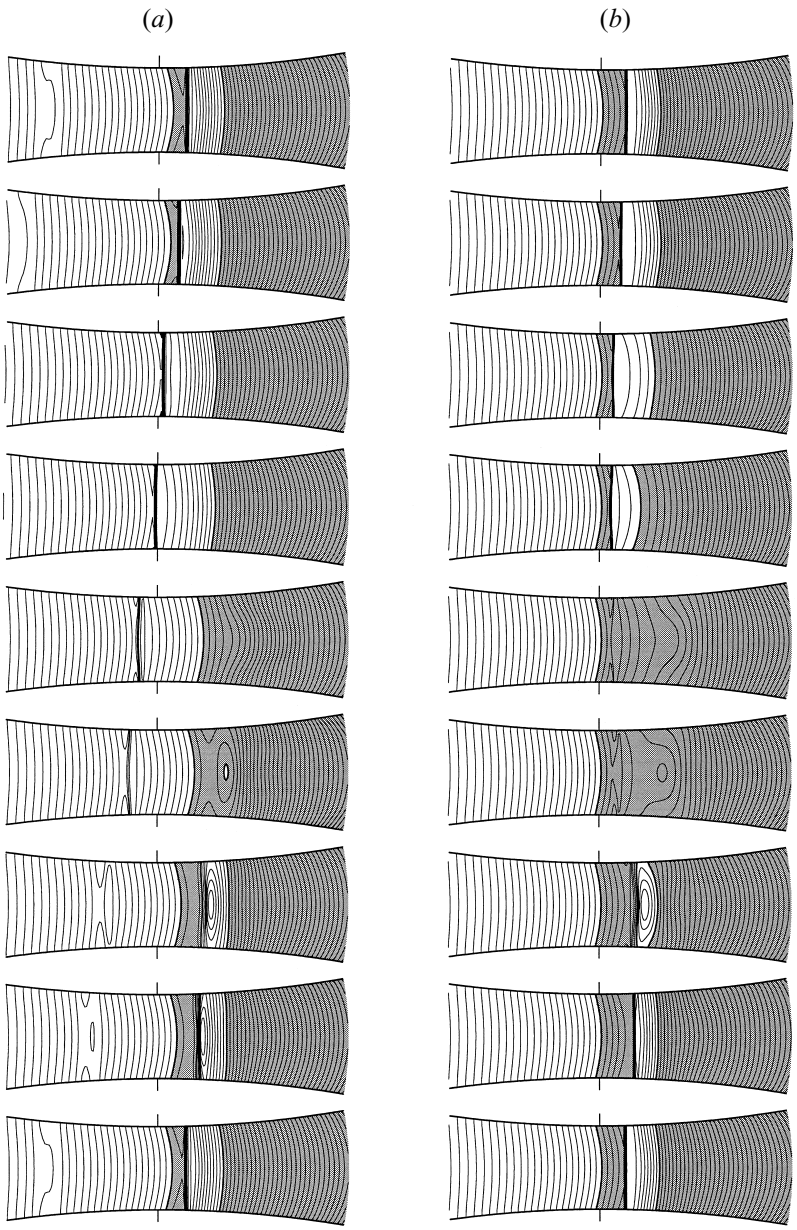

FIGURE 3. Oscillation modes 1 and 2 in slender circular arc nozzle S2, frozen Mach number M_f, increment of the iso-lines $\Delta M_f = 0.02$, grey $M_f > 1$; $T_{01} = 295$ K, $p_{01} = 1.0$ bar (*a*) mode 1, $\Phi_0 = 90\,\%$, $x = 15.0\ g_{H_2O}/kg_{dry\ air}$, $f = 1122$ Hz,; (*b*) mode 2, $\Phi_0 = 73.5\,\%$, $x = 12.2\ g_{H_2O}/kg_{dry\ air}$, $f = 677$ Hz.

weakens as it returns in the main flow direction and dies out while a new shock forms downstream. In this case only the divergent nozzle section is affected by the flow oscillation and the mass flow rate remains constant. Detailed numerical investigations show that the frequency minimum in figure 1 exactly separates the flow oscillations of modes 1 and 2.

At the right the streak sequence shows an oscillation just above the stability limit

for steady-state flow (mode 3). Here no periodic shock formation is visible except an oscillation of one single shock with nearly constant strength. In mode 3 the frequency strongly increases in comparison with mode 2 (figure 1) and we assume that the transition to steady-state flow takes place with finite frequency but vanishing amplitude of the shock motion.

The numerical simulations in figure 3 of oscillation modes 1 and 2 emphasize the quasi-one-dimensional structure of the flow field in this nozzle with nearly normal shocks. In mode 1 the stronger shock which moves into the convergent nozzle section causes a stronger decrease of the nucleation and condensate formation for a short time, but the high water vapour content in the flow immediately results in the formation of a new condensation zone downstream. In comparison the duration of interaction between shock and nucleation within the period is longer in mode 2 because the shock remains near the nozzle throat, i.e. within the nucleation zone. Owing to the strong heat release and the divergence of the nozzle shape the flow is again accelerated back to supersonic speed downstream of the shock in both cases, i.e. three sonic points are traversed in the flow direction.

6. Wall curvature effects

In order to investigate the influence of two-dimensional wave phenomena in unsteady condensing flows, we have used circular arc nozzles with the same cooling rate as nozzle S2 (according to one-dimensional theory), but with higher wall curvature. The extreme situation with strong two-dimensional effects is shown in figure 4 for nozzle S1 with a complex system of shocks and compression waves. Here the flow oscillation and the unsteady shock formation is concentrated near the centreline of the nozzle. Near the nozzle walls the locally stronger temperature gradient tends to stabilize the flow, only a weak shock develops just ahead of the nozzle throat at $t = 0.5\,T$. Downstream the flow is nearly in steady state. Near the nozzle axis the strong preceding shock and the compression waves caused by condensation emanating from the wall region tend to decrease the Mach number and subsequently the supersaturation. Thus the formation of the next shock is shifted downstream ($t = 0.375\,T$). Ahead of the shock the maximum Mach number at the centreline is only 1.03; behind a subsonic bubble-shaped area builds up for $0.375\,T \leqslant t \leqslant 0.875\,T$, which does not reach up to the nozzle walls, which again emphasizes the decoupling between the dynamics of near-wall regions and regions near the centreline.

7. Bifurcation and unsymmetric oscillations

7.1. *Comparison of steady diabatic flow in nozzles S2 and A1*

With respect to technical applications nozzles designed for a constant exit Mach number are important. In contrast to circular arc nozzles, where the temperature gradient $-\mathrm{d}T/\mathrm{d}x$ is nearly constant up to the condensation region, it monotonically decreases in such nozzles to zero at the nozzle exit. Figure 5 schematically shows the geometry and the Mach number along the centreline of nozzle A1. In diabatic flow the small divergence of the geometry restricts the heat which can be released to the flow subcritically, i.e. without shock, to a very low value. Thus the supercritical flow pattern with a shock is already established at very low values of $\Phi_0 \approx 30\%$, where only a very weak compression is observed for circular arc nozzles. There the supercritical flow pattern occurs only for much higher water-vapour content in

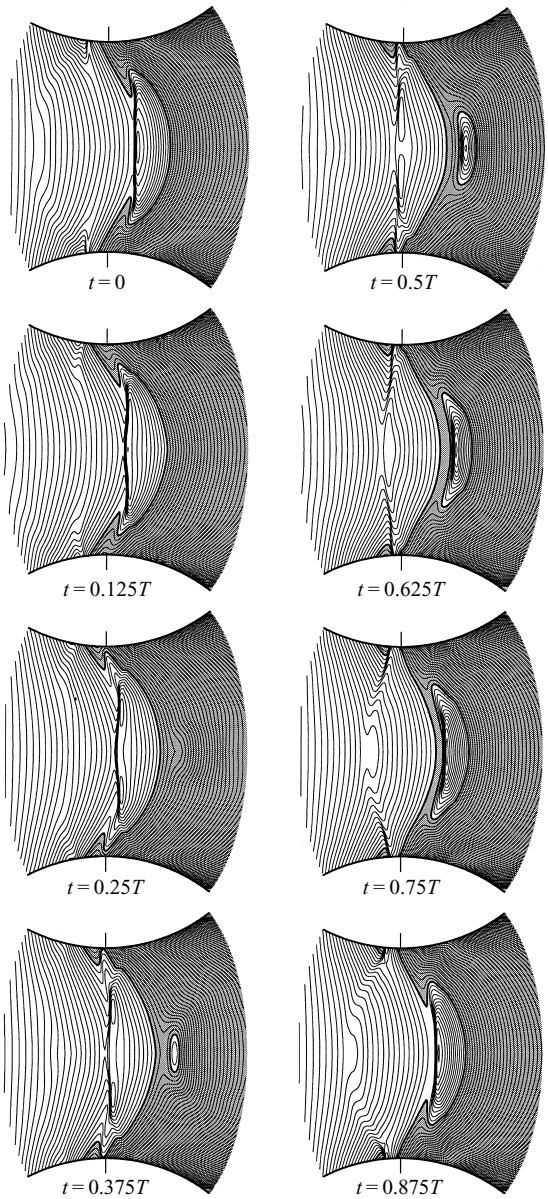

FIGURE 4. Self-excited flow oscillation in strongly curved circular arc nozzle S1, frozen Mach number M_f, increment of the iso-lines $\Delta M_f = 0.02$, grey $M_f > 1$. Reservoir conditions $T_{01} = 295\,\mathrm{K}$, $p_{01} = 1.0$ bar, $\Phi_0 = 90\%$, frequency $f = 1106$ Hz.

the flow with $\Phi_0 \approx 70\%$. The comparison of the two-dimensional flow field with supercritical (steady) heat addition in nozzles S2 and A1 is shown in figure 6. Owing to the much higher value of Φ_0, the Mach number ahead of the shock in nozzle S2 ($M = 1.09$) is lower than in nozzle A1 ($M = 1.16$), in spite of the higher cooling rate. The lower nucleation rate ahead of the shock, leading to fewer droplets, and the lower growth of the droplets downstream result in a lower release of heat to the flow in nozzle A1. This can be clearly seen by the distance between the shock and the onset of condensation (the $g/g_{max} = 0.05$ contour) and the slow increase of

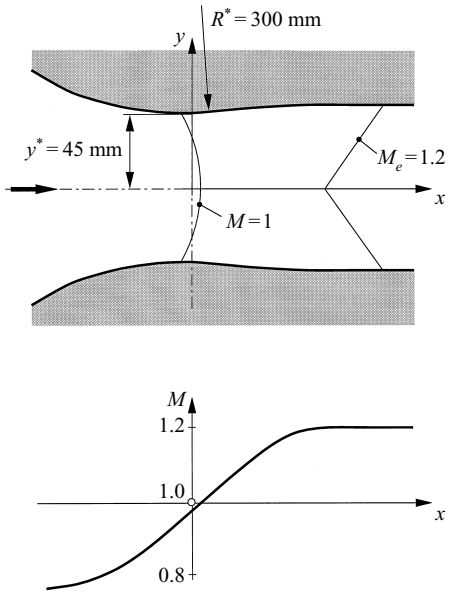

FIGURE 5. Geometry and nonlinear Mach number variation along the axis of nozzle A1.

g/g_{max}. Obviously the heat release in the divergent nozzle part is not strong enough to accelerate the flow to supersonic speed. Therefore, the flow remains subsonic up to the nozzle exit, where it reaches sonic speed. This is a characteristic difference from the flow in the circular arc nozzle S2, where an acceleration to supersonic speed takes place behind the shock.

In both nozzles the shock is almost normal whereas the constant Mach number contours clearly depict two-dimensional structures. This causes different values of the nucleation rate J at the nozzle wall and the nozzle axis, respectively, because J only depends on the thermodynamic state and therefore is constant for a given Mach number.

In nozzle S2 the nucleation rate J increases toward the wall just ahead of the shock and the condensate mass fraction increases toward the wall, too. In nozzle A1 the curvature of the constant-Mach-number contours changes its sign ahead of the shock, which causes the opposite tendency: J and therefore g/g_{max} decrease toward the nozzle wall.

7.2. *Periodic flow oscillations in nozzle A1 – bifurcation*

A steady-state flow pattern as shown in figure 6 only exists below $\Phi_0 \approx 40\%$ in nozzle A1. Then the flow becomes unsteady, similar to circular arc nozzles. However, the experimentally determined variation of the frequency with Φ_0 does not compare with any of our previous results, figure 7. There are two separate branches in totally different frequency regimes. It was found that the frequency jumps by a factor 2 or more at a certain threshold value of Φ_0. Along both branches the frequency changes less compared to circular arc nozzles. Also there is only a weak sensitivity on the reservoir temperature T_{01}.

The schlieren pictures in figure 8 of one flow oscillation of each branch reveal the background for this frequency bifurcation. The left-hand sequence shows an oscillation of the lower branch, indicated by the left-hand arrow in figure 7. It represents what was to be expected, a symmetric oscillation, very similar to mode 1 discussed before

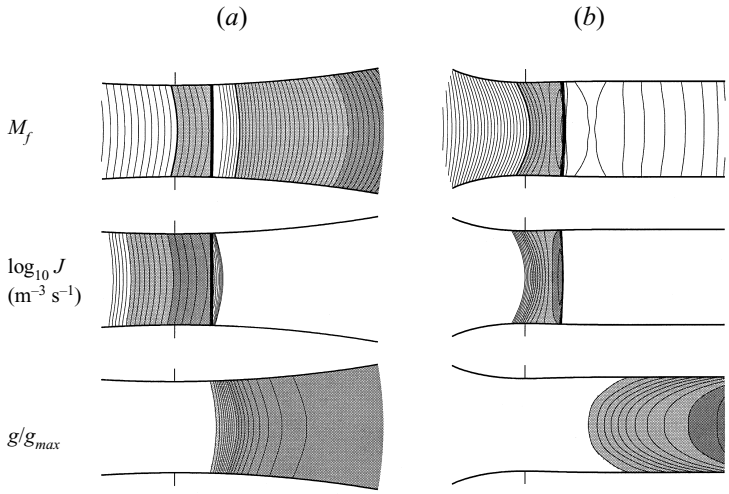

FIGURE 6. Comparison of steady-state flow with supercritical heat addition, (*a*) nozzle S2, $T_{01} = 287.2$ K, $p_{01} = 1.0$ bar, $\Phi_0 = 73.4\%$, $x = 7.3$ $g_{H_2O}/kg_{dry\ air}$, (*b*) nozzle A1, $T_{01} = 298.7$ K, $p_{01} = 1.0$ bar, $\Phi_0 = 35.6\%$, $x = 7.3$ $g_{H_2O}/kg_{dry\ air}$.

		light grey	dark grey	increment
Frozen Mach number (top)	M_f	> 1	> 1.5	0.02
Nucleation rate (middle)	$\log_{10} J$ [$m^{-3}s^{-1}$]	> 10	> 18	1
Condensate mass fraction (bottom)	g/g_{max}	> 0.05	> 0.5	0.05

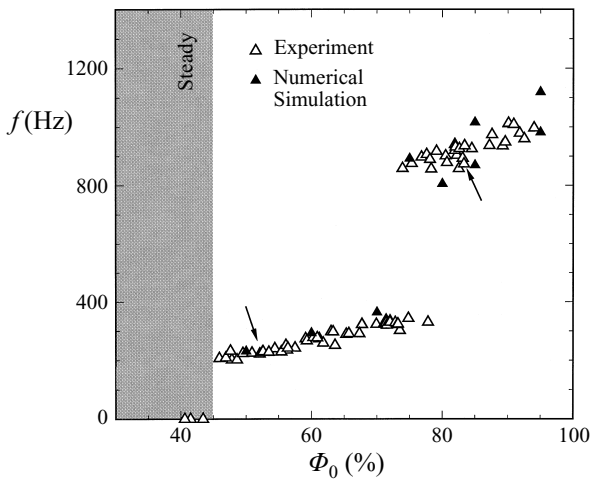

FIGURE 7. Frequency dependence on the relative humidity in the reservoir Φ_0 in nozzle A1 – experimental results compared to some numerical simulations. Lower branch: experiment $287.5 \leqslant T_{01} \leqslant 305$ K, numerical simulation 300 K, upper branch: experiment $285.5 \leqslant T_{01} \leqslant 295$ K, numerical simulation 285, 295 K.

for nozzle S2. The right-hand sequence of an oscillation in the upper frequency regime shows a phenomenon which had not yet been observed. A complex system of oblique shocks forms periodically and moves through the nozzle opposite to the main flow direction. The flow is no longer symmetrical with respect to the nozzle axis. In the region of the nozzle throat an unsteady Mach reflection occurs before the furthest upstream shock becomes more and more curved and separates from the remaining

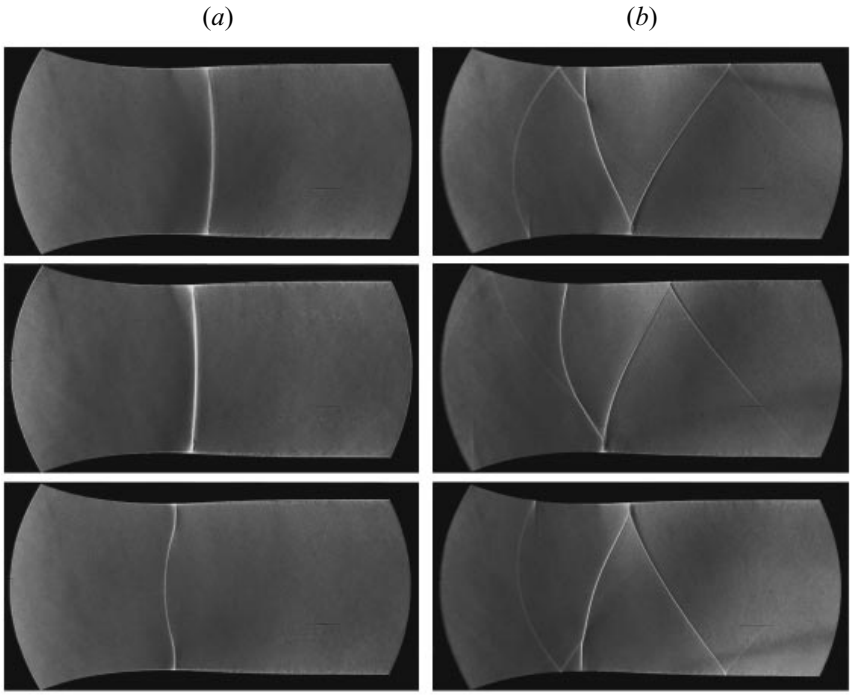

FIGURE 8. Experiment – bifurcation in nozzle A1, schlieren pictures of symmetric and unsymmetric flow oscillation: (*a*) symmetric mode, $f = 225$ Hz, $T_{01} = 292.8$ K, $p_{01} = 1.0$ bar, $\Phi_0 = 51.6\%$, $x = 7.4\ g_{H_2O}/kg_{dry\ air}$; (*b*) unsymmetric mode, $f = 905$ Hz, $T_{01} = 288.2$ K, $p_{01} = 1.0$ bar, $\Phi_0 = 82.0\%$, $x = 8.8\ g_{H_2O}/kg_{dry\ air}$.

shock system. It weakens and dies out as it accelerates into the oncoming flow. The process repeats alternately at the upper and the lower nozzle wall.

Of course, there are always disturbances in experiments, e.g. inhomogeneities of the oncoming flow, no perfectly symmetric nozzle contours, slight back pressure fluctuations downstream. Also the shock–boundary layer interaction could cause small unsteady separation bubbles, not visible in the schlieren pictures above. From that point of view it could not be guaranteed by our experiments shown alone that the bifurcation is definitely caused by the interaction of flow and phase transition processes and not by viscous effects or slightly imperfect conditions.

Numerical simulations of the flow with the Euler equations should clarify these uncertainties. It was found that all the results of the experiments are very well reproduced by the inviscid calculations. Here the computational grid and the code used are perfectly symmetric with respect to the nozzle axis and the oncoming flow is absolutely homogeneous. Moreover, it will be shown below that the numerical viscosity and the boundary condition at the outlet of the nozzle have no effect on the unsymmetric flow pattern and the existence of the bifurcation. Hence, the reason for bifurcation and unsymmetric oscillation lies in the instability of the interaction of the transonic flow with the process of homogeneous condensation.

Furthermore it was found in the numerical simulations that the lower branch of the frequency curve exists even beyond the bifurcation point found in the experiments. This means that up to another threshold value of Φ_0 both oscillation modes, symmetric

and unsymmetric, are possible at identical reservoir conditions and the frequency distribution clearly depicts hysteresis (figure 1).

Figure 9 shows a comparison of the symmetric and unsymmetric oscillations in the hysteresis regime at identical reservoir conditions. All details of the time-dependent two-dimensional flow field are in excellent agreement with the experimental results.

Figure 9(*a*) shows the dimensionless pressure disturbance with respect to steady adiabatic flow $(p-p_{ad})/p_{01}$. In both cases there is a significant pressure increase visible with higher maximum values in the unsymmetric case (27% of the reservoir pressure p_{01}). In contrast to the stabilization effect in strongly curved nozzles the unsymmetric oscillation causes the opposite effect. Now the maximum pressure disturbance is concentrated near the nozzle walls, which may be of great importance to dynamical forces and flutter excitation in technical applications like turbomachinery.

Figure 9(*b*) shows a very complex structure of the nucleation rate $\log_{10} J$ $(\mathrm{m}^{-3}\mathrm{s}^{-1})$ during the unsymmetric oscillation caused by the interaction with the upstream-moving shock system. As the Mach stem develops near the wall it cuts the nucleation rate off, whereas a low number of condensation nuclei are formed during the whole period near the nozzle centreline. Compared to the symmetric oscillation the maximum value of $\log_{10} J \approx 20$ is nearly constant within the period, whereas it changes between 16 and 20 in the symmetric mode. In both cases the maximum nucleation rates are reached near the nozzle wall which leads to stronger condensate formation than near the nozzle axis (normalized condensate mass fraction g/g_{max} in figure 9*c*). In the symmetric mode the condensation zone builds up starting from regions near the walls before it is shifted toward the nozzle exit by convection. Momentarily the nozzle is completely free of condensate before the next period starts. At the right the condensation zones are formed alternately near the upper and lower nozzle wall, but here a new condensation front forms as the downstream-moving front is still ahead of the nozzle exit (second picture from top, lower nozzle wall). In both modes only about 60% of the water vapour is condensed at the nozzle exit. Owing to the small divergence of the nozzle geometry the flow remains subsonic up to the exit where $M_f = 1$ is reached (figure 9*d*), whereas the flow is always accelerated to supersonic speed downstream of the shock in circular arc nozzles. This corresponds to steady-state flow (figure 6). The lower Mach number and hence the higher pressure and temperature suppress the strong droplet growth, which leads to lower values of g/g_{max}.

Another important difference of the symmetric oscillation compared to circular arc nozzles is the very low frequency (448 Hz), which is only about 40% of the value for nozzle S2 at the same reservoir conditions. First this is caused by the lower temperature gradient leading to lower supersaturation and nucleation rates as well as slower droplet growth. But secondly the condensate moving downstream, which acts similar to a displacement effect, keeps the flow near the throat at low velocities. This holds until the condensate is shifted out of the nozzle by convection. Then the flow near the throat again accelerates and a new zone of intense nucleation and condensate formation builds up, leading to a new shock. Of course this interaction between the downstream-moving condensate and the flow near the throat is only

FIGURE 9. Symmetric and unsymmetric flow oscillation for identical reservoir conditions $T_{01} = 295$ K, $p_{01} = 1.0$ bar, $\Phi_0 = 90.0\%$, $x = 15.0\ \mathrm{g}_{H_2O}/\mathrm{kg}_{dry\ air}$ in nozzle A1: (*a*) pressure disturbance with respect to the adiabatic flow; (*b*) nucleation rate; (*c*) condensate mass fraction; (*d*) frozen Mach number. Frequencies: symmetric 447 Hz, unsymmetric 1068 Hz.

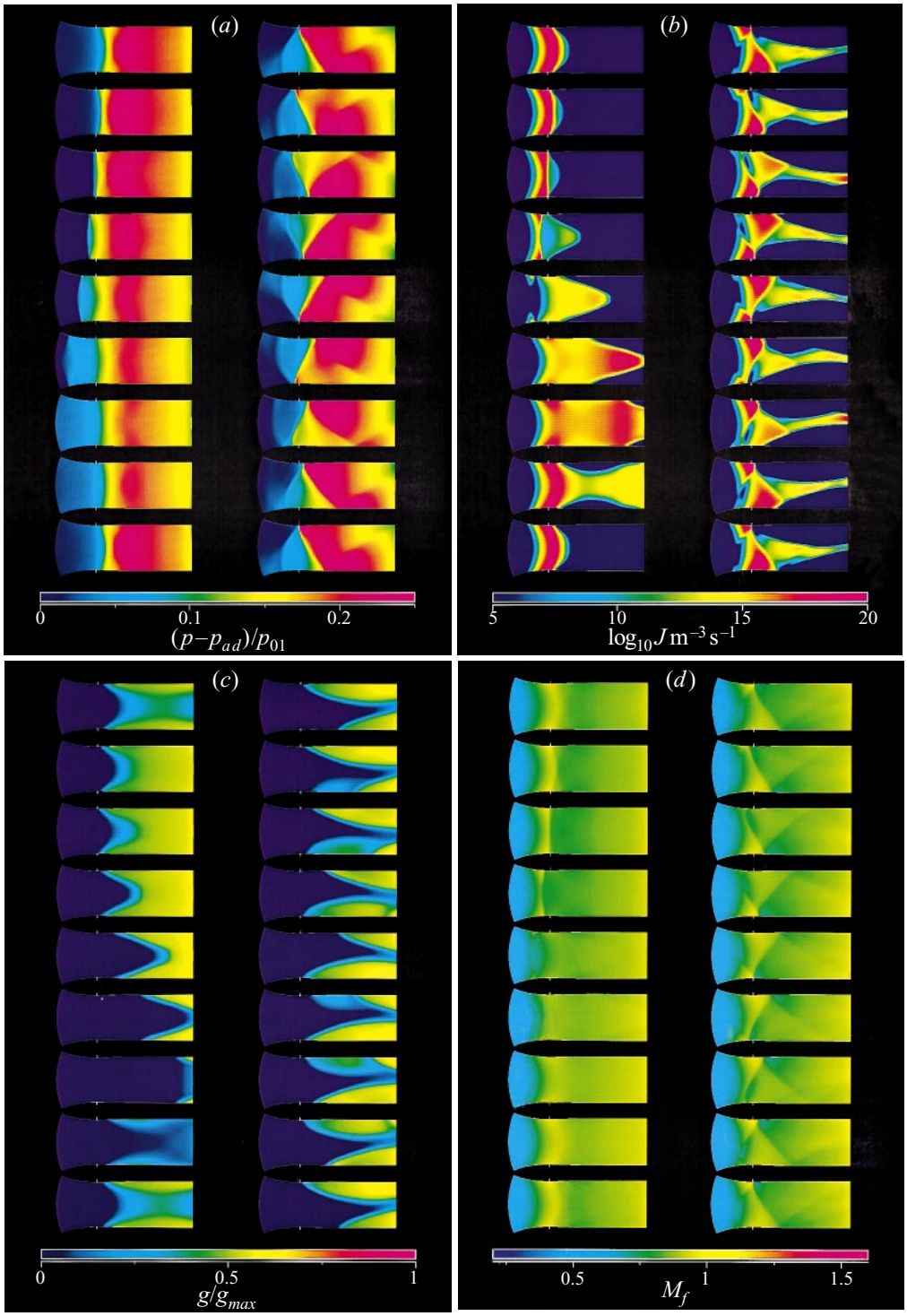

FIGURE 9 (*a–d*). For caption see facing page.

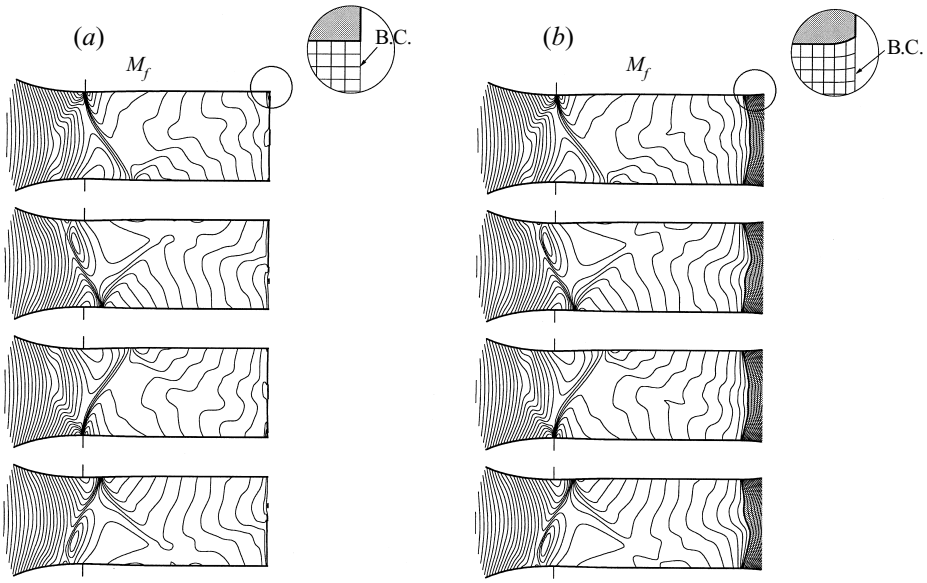

FIGURE 9. Unsymmetric flow oscillation (reservoir conditions as in figure 9 with different outflow boundary conditions – subsonic outflow with constant exit pressure (*a*), supersonic outflow (*b*).

possible in subsonic flow, i.e. it has almost no effect in circular arc nozzles where acceleration to supersonic speed takes place almost immediately behind the shock.

In the experiments the nozzle ends after the parallel duct, i.e. the cross-sectional area is discontinuously increased. Therefore, centred Prandtl–Meyer-expansions develop at the outlet leading to supersonic flow. In order to investigate the influence of the outflow boundary condition in the numerical simulation, we calculated unsymmetric flow oscillations in the nozzles shown in figure 9. In part (*a*) the geometry is cut off at the end of the parallel part. Here the flow remains subsonic; at the outflow boundary the Mach number is nearly unity. Thus a constant static pressure was prescribed as outflow boundary condition. In part (*b*) the nozzle was lengthened with a small divergent part leading to supersonic outflow. Now the interior flow field is independent of the outflow boundary. Comparison of both oscillations shows that a difference only occurs near the nozzle exit. The upstream flow field, above all the structure of the oblique shock system and the frequency, remains unchanged.

8. Transient rearrangement of symmetric to unsymmetric instabilities

As was mentioned above, the coexistence of symmetric and unsymmetric oscillations at identical reservoir conditions is only possible up to a further stability limit (figure 1*c*). Then, the numerical simulation initialized with the steady adiabatic flow solution yields only unsymmetric oscillations. It could be objected that this is caused by stronger disturbances during the transient phase at the beginning of the calculation when suddenly a large amount of heat is released to the supersonic flow. However, figures 10 and 11 clearly show that there is another physical instability leading to the development of the unsymmetric oscillation. Here the reservoir temperature was chosen higher, $T_{01} = 305$ K, because the effects are more distinctive.

Up to a relative humidity $\Phi_0 = 75\%$ a symmetric oscillation is established, which is indicated by the pressure oscillation at the nozzle throat in figure 10(*a*). The period of

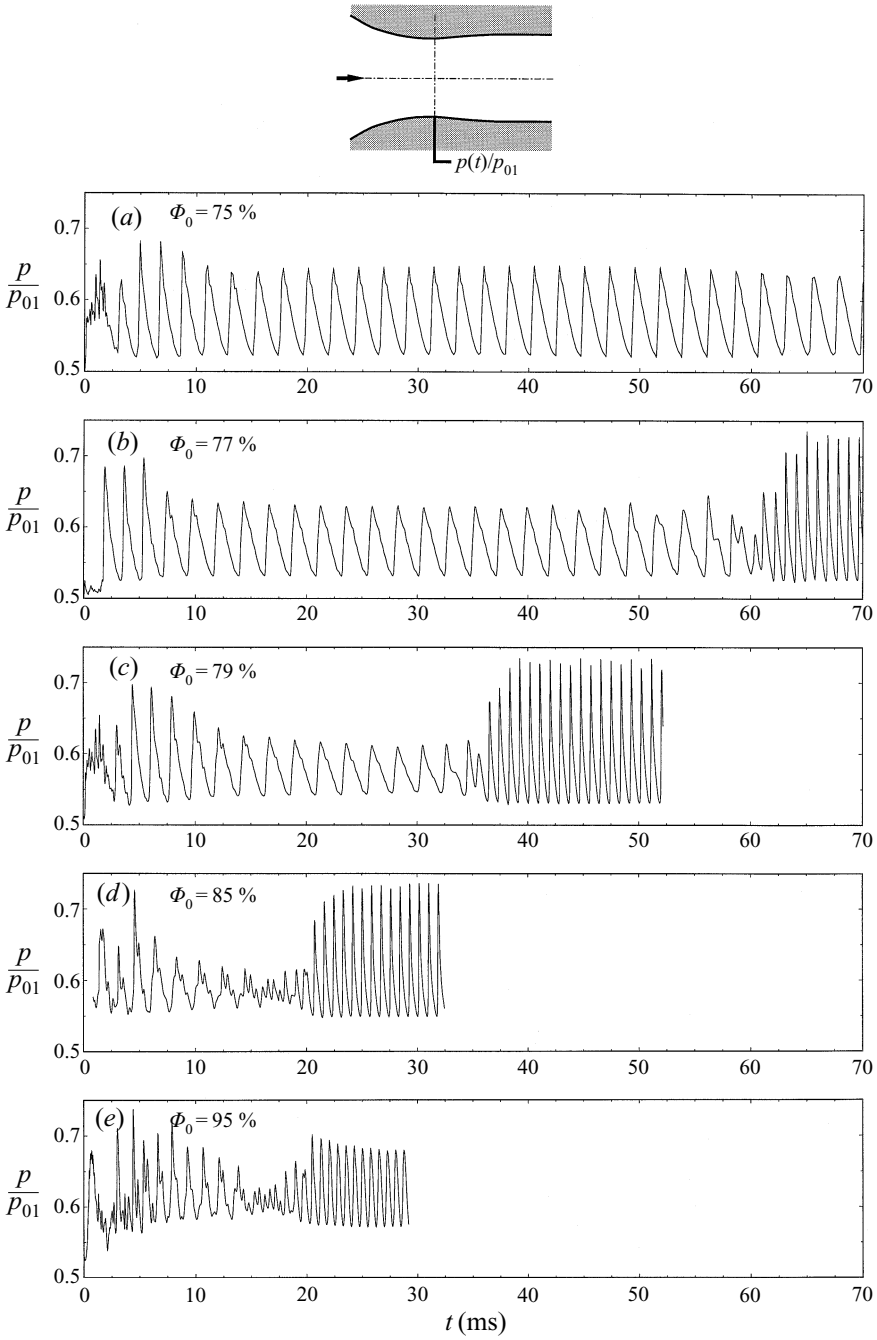

FIGURE 10. Transient rearrangement from symmetric to unsymmetric flow oscillations for different relative humidities in the reservoir Φ_0 ($T_{01} = 305$ K).

$T = 2.27$ ms corresponding to a typically low frequency $f = 440$ Hz remains stable. Only a small regime of the calculation up to $t = 180$ ms is shown. For $\Phi_0 = 77\%$ a new phenomenon is observed. First a symmetric oscillation builds up before suddenly the oscillation period gets much shorter and the pressure amplitude increases. The

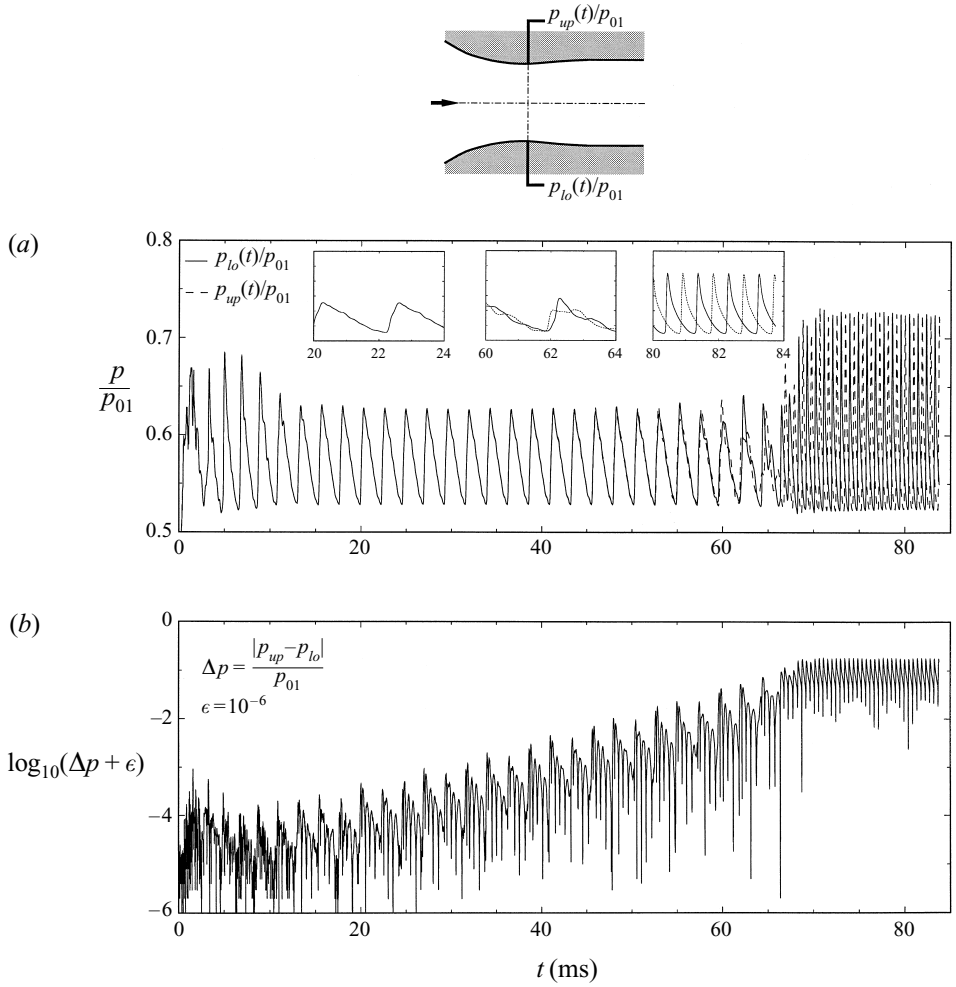

FIGURE 11. Transient rearrangement from symmetric to unsymmetric flow oscillation – exponential growth of pressure disturbance in unstable symmetric flow oscillation.

reason for this is a sudden rearrangement of the whole flow field, which gets into the unsymmetric mode and now remains stable. As expected the duration of the transient process decreases with increasing Φ_0. For $\Phi_0 \geqslant 85\%$ the symmetric oscillation is strongly superposed by aperiodic pressure fluctuations typical for the beginning of the calculation. What is important is that near the stability limit above $\Phi_0 = 75\%$ the unsymmetric solutions are not produced by these pressure waves. Moreover, a comparison of the time-dependent pressure at the upper and lower nozzle wall for $\Phi_0 = 77\%$ confirms a new instability (figure 11). Part (*a*) depicts identical pressure curves in the symmetric mode ($20 \leqslant t \leqslant 24$ ms) and a shift of the curves of half a period in the unsymmetric mode ($80 \leqslant t \leqslant 84$ ms). Between the fully developed symmetric and unsymmetric oscillation the logarithmic pressure difference between the upper and the lower nozzle wall $\log_{10}|(p_{up} - p_{lo})/p_{01} + \epsilon|$ shows a characteristic growth of disturbances. The quantity $\epsilon = 10^{-6}$ was added to prevent the argument of the logarithm from being zero. At the beginning of the calculation the initial aperiodic pressure fluctuations are damped out very quickly ($t < 10$ ms). Then, as

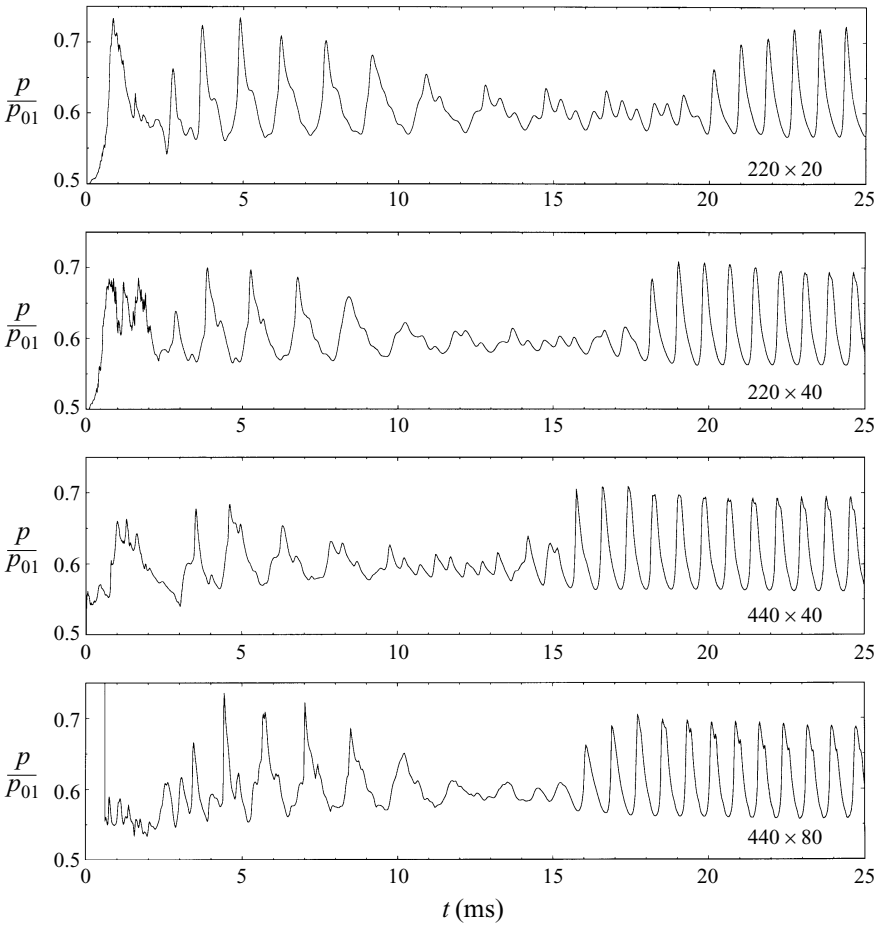

FIGURE 12. Transient rearrangement from symmetric to unsymmetric flow oscillations ($T_{01} = 305$ K, $\Phi_0 = 90\%$) – dependence on grid refinement.

the flow is oscillating symmetrically with constant frequency $f = 430$ Hz, small disturbances of the order 10^{-5} start to be amplified. This transient phase, where we observe an approximately linear increase of $\log_{10}|\Delta p/p_{01} + \epsilon|$, i.e. exponential growth of disturbances, is terminated when the fluctuations are of the order 10^{-1}. Now the whole flow field is rearranged and the unsymmetric oscillation with a frequency $f = 1073$ Hz is established.

The authors are aware of the fact that the numerical simulations certainly slightly alter the physical instability because the necessary artificial viscosity may damp out high-frequency disturbances and frequencies could be amplified, which are damped in the experiments due to the natural viscosity. More accurate amplification rates, stability limits and values for the regime of hysteresis could only be investigated with an analytical stability analysis of the Navier–Stokes equations coupled to the phase transition process. Extension of the asymptotic predictive method for gas dynamics with condensation (Delale, Schnerr & Zierep 1993*b*) to unsteady flow patterns could be the starting point for a stability analysis.

Nevertheless, we investigated the influence of grid refinement on the development of the unsymmetric solution on four different grids with $\Phi_0 = 90\%$ ($T_{01} = 305$ K).

	Cells in x-direction	Cells in y-direction	Frequency (Hz)	CPU-time to calculate transient process
(a)	220	20	1192	10 min
(b)	220	40	1270	20 min
(c)	440	40	1289	1.0 h
(d)	440	80	1299	2.2 h

TABLE 1. Transient rearrangement from symmetric to unsymmetric flow oscillations ($T_{01} = 305$ K, $\Phi_0 = 90\%$) – dependence of frequency and CPU-time on grid refinement.

Apart from the very coarse grid with 220×20 cells the calculated oscillation frequency is nearly the same with less than 2.5% increase from the second grid (220×40), which was used in all previous simulations, to the finest grid with 440×80 cells, which requires a 13 times higher CPU-time (table 1).

The transient pressure curves for the lower wall at the nozzle throat in figure 12 indicate that the time until the unsymmetric oscillation develops is slightly shorter for the finest grids, i.e. the amplification of disturbances is slightly higher. This also holds for $\Phi_0 = 77\%$ where the transition to the unsymmetric mode has already occurred at $t = 53$ ms in the finest grid, whereas figure 11 yields $t = 67$ ms for the grid with 220×40 cells.

The trend in instability of symmetric oscillations above a threshold value of the water-vapour content is well confirmed by experiments. But there the inherent disturbances cause symmetric oscillations of the hysteresis regime, which are only weakly stable, to turn into the unsymmetric mode. Nevertheless, we registered a symmetric oscillation in the hysteresis regime, which seems to be stable for about 400 periods, before transition to the unsymmetric mode takes place. Five sequences of the high-speed movie in figure 13 show the rearrangement of the flow field from the symmetric to the unsymmetric mode. In column (a) the symmetric oscillation is already slightly disturbed. Five periods later (column b) and after three further periods (column c) the flow field is still oscillating with nearly the frequency of the symmetric mode before the transition to the unsymmetric mode takes place (columns d and e). Overall the transition takes about 20 periods, corresponding to about 60 ms, from the state where a macroscopic disturbance is visible to the fully developed unsymmetric mode.

An analytical stability analysis could lead to a detailed understanding of the mechanism which causes the instability of the symmetric oscillation. Our latest numerical investigations indicate that several conditions are necessary for the development of the unsymmetric mode. The heat added to the flow near the nozzle walls requires a certain intensity. Also the condensation zones near the walls and at the centreline of the nozzle have to be to some extent decoupled, i.e. in this case the condensation zone has a strongly two-dimensional shape (see condensate mass fraction g/g_{max} in figure 9). Furthermore, all of the yet investigated unsymmetric oscillations show that the interaction between the shock system and the condensation process takes place in the subsonic regime near Mach number unity. The effect of condensation in the absence of other influences normally is to reduce the supersaturation. However, within the Mach number regime $1/\gamma^{1/2} \leqslant M_f < 1$ it is actually possible that the supersaturation even increases through the heat release. It is well known that this effect also is responsible for another type of instability in steady flow through converging–diverging nozzles (Young 1984).

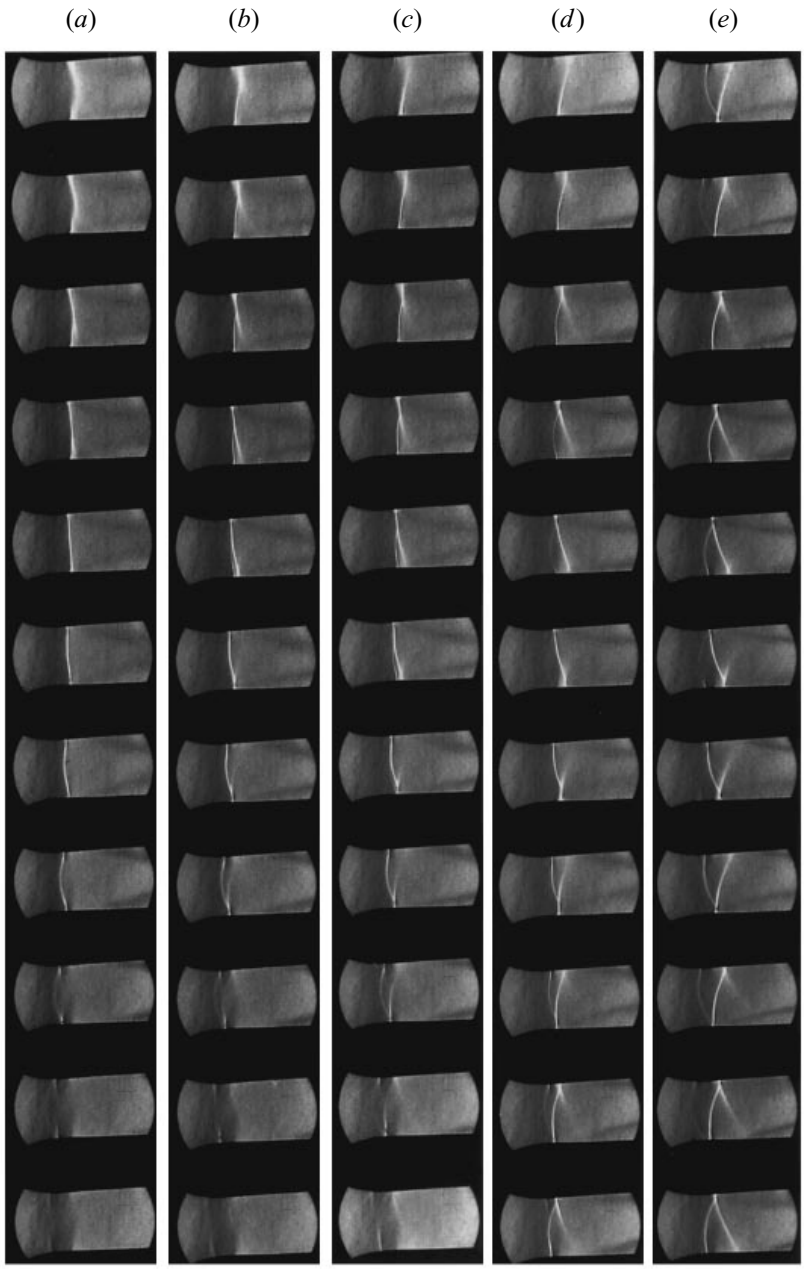

FIGURE 13. Experiment – transient rearrangement from symmetric to unsymmetric flow oscillation, high-speed movie with 7000 pps (time increases from top); reservoir conditions: $T_{01} = 290.6$ K, $p_{01} = 1.0$ bar, $\Phi_0 = 77.1\%$, $x = 9.8\ g_{H_2O}/kg_{dry\ air}$; frequencies: 333 Hz (fully developed symmetric oscillation), 897 Hz (fully developed unsymmetric oscillation).

Finally, the numerical simulations as well as the high-speed movie show that during the transient rearrangement of the flow field compression waves are travelling perpendicularly to the main flow direction between the lower and upper nozzle wall. These waves, i.e. perturbances, seem to be amplified if their characteristic timescale

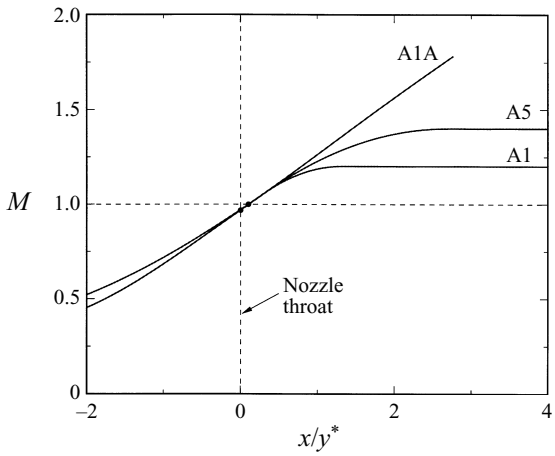

FIGURE 14. Mach number in isentropic flow along the centerline of nozzles A1, A5, and A1A with throat height $2y^* = 90$ mm, $R^* = 300$ mm.

is such that the waves cross the nozzle height twice within a symmetric oscillation period.

In which way these different phenomena – amount and decoupling of heat release, Mach number regime, and pressure waves between the nozzle walls – act together in the unsteady two-phase flow field and result in the instability is a subject of future work. It cannot be completely understood by the investigations carried out so far.

9. Bifurcation in circular arc nozzles

In the previous discussions of bifurcation and unsymmetric flow pattern the nozzle geometry was kept constant. In order to prove that these phenomena are not restricted to nozzle A1 or other nozzles with extremely slender divergent parts, we continuously increased the ratio of the cross-sectional areas at the nozzle exit and the nozzle throat. The throat height $2y^* = 90$ mm and the wall curvature at the throat $R^* = 300$ mm are kept constant. Finally, we investigated the limiting case, i.e. a circular arc geometry with $2y^* = 90$ mm and $R^* = 300$ mm.

Figure 14 shows the frozen-Mach-number distribution along the centerline for three of these different examples. Nozzle A5 leads to a constant isentropic outflow Mach number 1.4. In the circular arc nozzle A1A the Mach number increases almost linearly toward the exit, which means that the temperature gradient $(-\mathrm{d}T/\mathrm{d}x)$ is nearly constant, whereas it nonlinearly decreases to zero in the other cases. Owing to the constancy of the parameter y^*R^* the acceleration near the nozzle throats is the same. Here, the temperature gradient according to one-dimensional theory is $(-\mathrm{d}T/\mathrm{d}x)^*_{1-D} = 5.34$ K cm^{-1}.

By means of an example we calculated the two-phase flow oscillation in all nozzles with identical reservoir conditions $T_{01} = 295$ K and $\Phi_0 = 90\%$, shown by the constant frozen-Mach-number contours in figure 15. Independent of the geometry we obtain a stable unsymmetric solution, which means that the stronger geometrical divergence does not prevent the bifurcation, even for the circular arc nozzle with nearly constant temperature gradient. This is an important generalization because now it has to be assumed that bifurcation could occur in arbitrary nozzle shapes. Additionally the unsymmetric flow pattern is independent of whether the flow is accelerated to

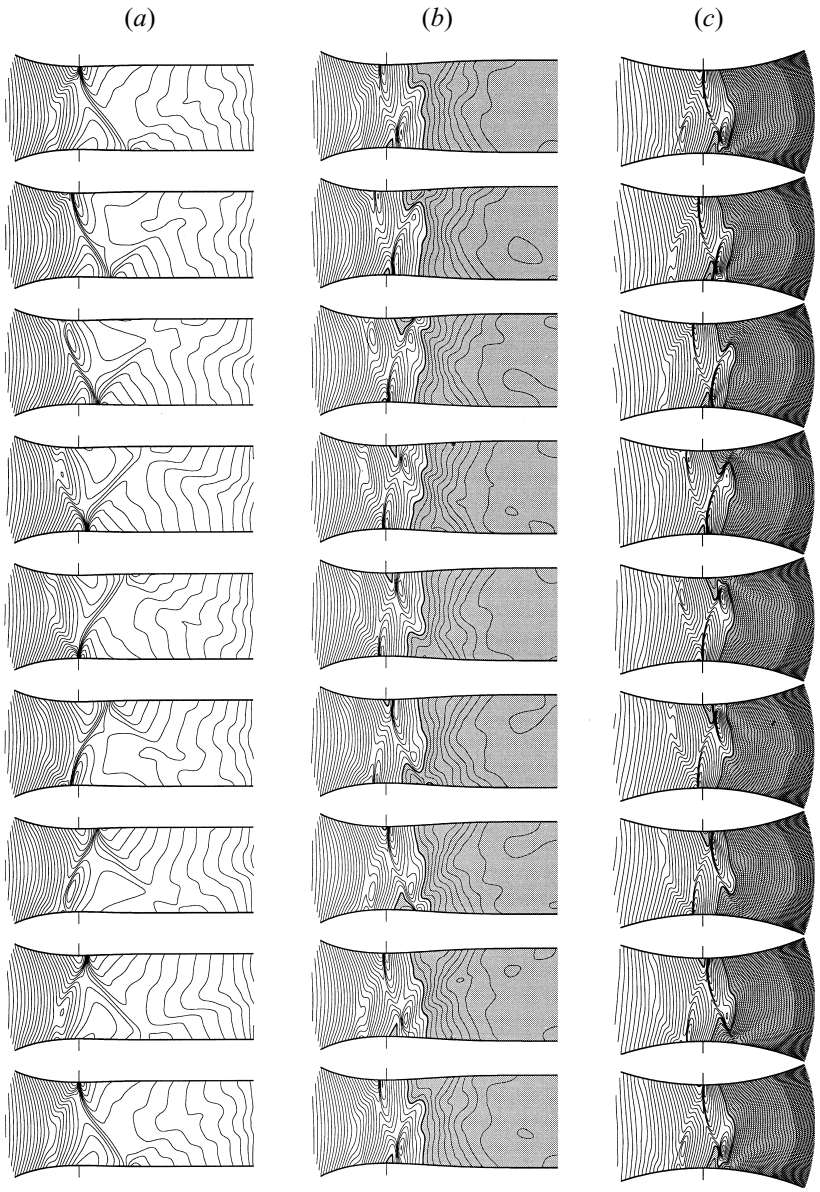

FIGURE 15. Unsymmetric oscillation in nozzles with increasing divergence $2y^* = 90$ mm, $R^* = 300$ mm; frozen Mach number M_f (increment $\Delta M_f = 0.02$, light grey: $M_f > 1$, dark grey: $M_f > 1.5$); reservoir conditions $T_{01} = 295$ K, $p_{01} = 1.0$ bar, $\Phi_0 = 90\%$, $x = 15.0\ g_{H_2O}/kg_{dry\ air}$. (*a*) Nozzle A1, isentropic outflow Mach number $M_{e,is.} = 1.2$, frequency $f = 1068$ Hz; (*b*) nozzle A5, $M_{e,is.} = 1.4$, $f = 1105$ Hz; (*c*) circular arc nozzle A1A, $f = 1140$ Hz.

supersonic speed by the heat release (nozzles A5 and A1A) or remains subsonic (nozzle A1). Therefore, the instability is controlled by the interaction of flow and phase transition processes near the nozzle throat, independent of the downstream conditions.

As expected the frequency slightly increases with increasing divergence because the mean temperature gradient becomes higher. In nozzles A5 and A1A the coupling of

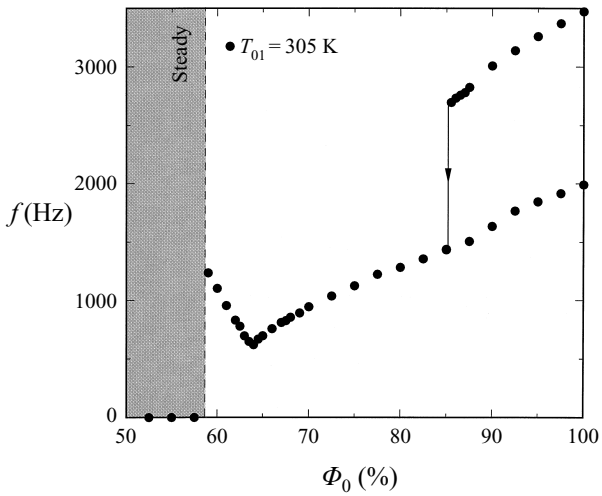

FIGURE 16. Bifurcation of frequency in slender circular arc nozzle S2.

the stronger heat release and the acceleration of the flow behind the shocks leads to steeper shocks than in nozzle A1. Also a new compression zone leading to a subsequent shock is formed in the region between nozzle wall and centreline, whereas it is generated at the wall in nozzle A1.

The last diagram, figure 17 shows that the characteristic bifurcation structure even develops in nozzle S2 with higher temperature gradient $(-\mathrm{d}T/\mathrm{d}x)^*_{1-D} = 8.14$ K cm^{-1}, which additionally is very slender compared to the circular arc nozzle A1A. Of course, the frequencies obtained by numerical simulations are much higher here. The only differences to nozzle A1 are that the bifurcation occurs for higher reservoir temperatures, here $T_{01} = 305$ K, and that the frequency increase at the bifurcation point is only 88%, which is caused by decoupling of the oscillation near the nozzle walls and the centreline (Adam 1996). The gradient of the lower branch of the frequency curve to the left and right of the minimum is nearly the same as for the lower reservoir temperature, i.e. $T_{01} = 295$ K in figure 1. Owing to the higher water vapour content at the same value of Φ_0 the onset of self-excited flow oscillations and the minimum are shifted to lower values of Φ_0.

In principle all characteristic phenomena, bifurcation, unsymmetric oscillation, and hysteresis, are reproduced in this slender circular arc nozzle. This emphasizes the ansatz that this instability exists in arbitrary nozzle geometries.

10. Conclusions

Homogeneous condensing nozzle flows are not only a very elegant tool for investigation of high-speed compressible flows with internal heat addition, but they also represent an appropriate physical model for investigation of instabilities and bifurcations of inviscid flows. All our results, i.e. the perfect agreement between experiment and numerical simulation based on the Euler equations, confirm that the existence of the bifurcation of the frequency curve and the formation of unsymmetric oscillating flow patterns is not controlled by viscous effects and is independent of grid refinements, variations of the cooling rate, and of sub- or supersonic flow conditions at the exit of the nozzle.

Because this new instability is not restricted to a limited class of nozzle shapes we expect additional higher-order two-dimensional and three-dimensional instabilities when increasing the amount of heat added to the flow or changing to practically important axisymmetric nozzles.

The existence of instabilities of such a highly nonlinear dynamical system is not unexepected. Similarity considerations, not included here, indicate that the dynamics of the frequency dependence at the bifurcaction points depends on travelling waves between the upper and lower nozzle wall. For other fluid dynamic problems such as Taylor–Görtler flows many different flow patterns exist. However and in contrast to our actual flow problem, there viscosity plays an important role.

As one of the next steps we are actually introducing unsymmetric boundary conditions, which are important to technical applications like cascade flows. It will be interesting to investigate what kind of bifurcations can be found under these conditions, where basically no symmetric flow pattern exists.

The authors would like to express their gratitude to the Deutsche Forschungsgemeinschaft for supporting our experimental and theoretical/numerical research on unsteady condensing flows through the contract Schn 352/13-3 – /13-5.

REFERENCES

Adam, S. 1996 Numerische und experimentelle Untersuchung instationärer Düsenströmungen mit Energiezufuhr durch homogene Kondensation. Dissertation, Fakultät für Maschinenbau, Universität Karlsruhe (TH), Germany

Anderson, W. K., Thomas, J. L. & Leer, B. van 1986 Comparison of finite volume flux vector splittings for the Euler equations. *AIAA J*. **24**, 1453–1460.

Barschdorff, D. 1967 Kurzzeitfeuchtemessung und ihre Anwendung bei Kondensationserscheinungen in Lavaldüsen. *Strömungsmechanik und Strömungsmaschinen* **6**, 18–39.

Barschdorff, D. 1971 Verlauf der Zustandsgrößen und gasdynamische Zusammenhänge bei der spontanen Kondensation reinen Wasserdampfes in Lavaldüsen. *Forschung im Ingenieurwesen*, **37** (5), 146–157.

Barschdorff, D. & Filippov, G. A. 1970 Analysis of special conditions of the work of laval nozzles with local heat supply. *Heat Transfer – Sov. Res*. **2**, 76–87.

Collignan, B. 1994 Contribution à l'etude de la condensation instationnaire en ecoulement transsonique. PhD thesis, Université Pierre & Marie Curie, Paris, France.

Deconinck, H. & Struys, R. 1988 Consistent boundary conditions for cell centered upwind finite volume Euler solvers. In *Numerical Methods for Fluid Dynamics III* (ed. K. W. Morton & M. J. Baines). Clarendon.

Delale, C. F. & Schnerr, G. H. 1996 Transient effects of nucleation in steady and unsteady condensing flows. *Intl J. Multiphase Flows* **22**, 767–781.

Delale, C. F., Schnerr, G. H. & Zierep, J. 1993*a* Asymptotic solution of transonic nozzle flows with homogeneous condensation. I. Subcritical flows; II. Supercritical flows. *Phys. Fluids* A **5**, 2969–2995.

Delale, C. F., Schnerr, G. H. & Zierep, J. 1993*b* The mathematical theory of thermal choking in nozzle flows. *Z. Angew Math. Phys*. **44** (6), 943–976.

Deych, M. E., Filippov, G. A., Saltanov, G. A., Kurshakov, A. V., Kukushkin, A. N. & Nozdrin, G. N. 1974 Experimental study of unsteady phenomena in a flow of condensing vapor in nozzles. *Fluid Mechanics – Sov. Res*. **3**, 151–157.

Guha, A. & Young, J. B. 1991 Time-marching prediction of unsteady condensation phenomena due to supercritical heat addition. *IMechE* C423/057, 167–177.

Hill, P. G. 1966 Condensation of water vapor during supersonic expansion in nozzles. *J. Fluid Mech*. **25**, 593–620.

Matsuo, K., Kawagoe, S., Sonoda, K. & Setoguchi, T. 1983 Oscillations of laval nozzle flow with condensation, Part 1. *Bull. JSME* **26** (219), 1556–1562.

Matsuo, K., Kawagoe, S., Sonoda, K. & Setoguchi, T. 1985 Oscillations of laval nozzle flow with condensation, Part 2. *Bull. JSME* **28** (235), 88–93.

Mundinger, G. 1994 Numerische Simulation instationärer Lavaldüsenströmungen mit Energiezufuhr durch homogene Kondensation. Dissertation, Fakultät für Maschinenbau, Universität Karlsruhe (TH), Germany

Oran, E. S. & Boris, J. P. 1987 *Numerical Simulation of Reactive Flow*. Elsevier.

Peters, F. & Paikert, B. 1989 Nucleation and growth rates of homogeneously condensing water vapor in argon from shock tube experiments. *Exps. Fluids* **7**, 521–530.

Saltanov, G. A. & Tkalenko, R. A. 1975 Investigation of transonic unsteady-state flow in the presence of phase transformations. *Zh. Prikl. Mek. i Tek. Fiz. (USSR)* **6**, 42–48.

Schmidt, B. 1962 Beobachtungen über das Verhalten der durch Wasserdampfkondensation ausgelösten Störungen in einer Überschall-Windkanaldüse. Dissertation, Fakultät für Maschinenbau, Universität Karlsruhe (TH), Germany.

Schnerr, G. H. 1993 Transonic aerodynamics including strong effects from heat addition. *Computers Fluids* **22**, 103–116.

Schnerr, G. H., Adam, S., Lanzenberger, K. & Schulz, R. 1995 Multiphase flows: condensation and cavitation problems. Invited Review Article for the First Issue of *Computational Fluid Dynamics Review 1995* (ed. M. Hafez, K. Oshima), pp. 614–640. John Wiley & Sons.

Schnerr, G. H., Adam, S. & Mundinger, G. 1994*a* Frequency control of shock oscillations in high speed two-phase flow. In *Fourth Triennal Intl Symp. on Fluid Control, Measurement and Visualization (FLUCOME'94)* (ed. P. Hebrard). ENSAE Toulouse, France, vol. 2, pp. 957–962.

Schnerr, G. H., Adam, S. & Mundinger, G. 1994 New modes of periodic shock formation in compressible two-phase flows. In *IUTAM Symp. on Waves in Liquid/Gas and Liquid/Vapor Two-Phase Systems* (ed. S. Morioka & L. van Wijngaarden), pp. 377–386. Kluwer.

Schnerr, G. H. & Dohrmann, U. 1990 Transonic flow around airfoils with relaxation and energy supply by homogeneous condensation. *AIAA J.* **28**, 1187–1193.

Šejna, M. 1993 Numerical modelling of unsteady wet steam flow. *Z. Angew Math. Mech.* **73** (6), T578–T581.

Shuen, J. S., Liou, M. S. & Leer, B. van 1990 Inviscid flux-splitting algorithms for real gases with non-equilibrium chemistry. *J. Comput. Phys.* **90**, 371–395.

Skillings, S. A. & Jackson R. 1987 A robust time-marching solver for one-dimensional nucleating steam flows. *Heat Fluid Flow* **8**, 139–144.

Wegener, P. P. & Cagliostro, D. J. 1973 Periodic nozzle flow with heat addition. *Combust. Sci. Tech.* **6**, 269–277.

White, A. J. & Young J. B. 1993 A time-marching method for the prediction of two-dimensional, unsteady flows of condensing steam. *J. Propulsion Power* **9**, 579–587.

Young, J. B. 1984 Critical conditions and the choking mass flow rate in nonequilibrium wet steam flows. *ASME Paper* 84-WA/FE-12.

Zierep, J. & Lin, S. 1968 Ein Ähnlichkeitsgesetz für instationäre Kondensationsvorgänge in Lavaldüsen. *Forschung im Ingenieurwesen* **34** (4), 97–132.